Monthly Notices
of the
ROYAL ASTRONOMICAL SOCIETY

MNRAS **471,** 3668–3679 (2017)
Advance Access publication 2017 July 21

doi:10.1093/mnras/stx1856

The global mass functions of 35 Galactic globular clusters: I. Observational data and correlations with cluster parameters

A. Sollima[1]★ and H. Baumgardt[2]

[1]*INAF Osservatorio Astronomico di Bologna, via Gobetti 93/3, Bologna, I-40129, Italy*
[2]*School of Mathematics and Physics, University of Queensland, St Lucia, QLD 4072, Australia*

Accepted 2017 July 18. Received 2017 July 18; in original form 2017 June 1

ABSTRACT

We have derived the global mass functions of a sample of 35 Galactic globular clusters (GCs) by comparing deep *Hubble Space Telescope* photometry from the *globular clusters treasury project* (Sarajedini et al. 2007) with suitable multimass dynamical models. For a subset of 29 clusters with available radial velocity information, we were also able to determine dynamical parameters, mass-to-light ratios and the mass fraction of dark remnants. The derived global mass functions are well described by single power laws in the mass range $0.2 < m/\mathrm{M}_{\odot} < 0.8$ with mass function slopes $\alpha > -1$. Less-evolved clusters show deviations from a single-power law, indicating that the original shape of their mass distribution was not a power law. We find a tight anticorrelation between the present-day mass function slopes and the half-mass relaxation times, which can be understood if clusters started from the same universal initial mass function (IMF) and internal dynamical evolution is the main driver in shaping the present-day mass functions. Alternatively, IMF differences correlated with the present-day half-mass relaxation time are needed to explain the observed correlation. The large range of mass function slopes seen for our clusters implies that most GCs are dynamically highly evolved, a fact that seems difficult to reconcile with standard estimates for the dynamical evolution of clusters. The mass function slopes also correlate with the dark remnant fractions indicating a preferential retention of massive remnants in clusters subject to high mass-loss rates.

Key words: methods: numerical – techniques: photometric – techniques: radial velocities – stars: kinematics and dynamics – stars: luminosity function, mass function – globular clusters: general.

1 INTRODUCTION

One of the long-standing issues of stellar astrophysics is the understanding of the mechanisms determining the mass distribution of stars. This topic represents one of the central questions in the theory of star formation and has strong relevance for many areas of astrophysics. The original distribution of stellar masses, commonly referred to as the initial mass function (IMF), is indeed a key ingredient in models of stellar population synthesis, chemical evolution of clusters and galaxies, dynamical evolution of stellar systems and, in general, in any topic involving the role of baryons.

In this regard, the universality of the IMF, its shape and the parameters driving its hypothetical variation are questions still far from being completely understood from both a theoretical and an observational point of view. Indeed, many complex processes affect the efficiency of fragmentation of a molecular cloud (dependence of the Jeans mass from thermodynamical parameters, competitive accretion, metal line-driven cooling, etc., Silk 1977; Fleck 1982; Bonnell et al. 1997; Nakamura & Umemura 2001). A practical difficulty in observationally constraining the IMF resides in its temporal evolution, which strongly depends on the characteristics of the considered stellar population and on its environment. An ideal class of astrophysical objects where to perform an analysis of the IMF should be young, dynamically unevolved stellar populations containing a large number of coeval and chemically homogeneous stars covering a wide range of masses. None of the known star-forming complexes satisfy all the above requirements so, from the pioneering study by Salpeter (1955), many studies concentrated on the determination of the IMF shape in the Galactic field, in OB associations (Miller & Scalo 1979; Kroupa 2001; Chabrier 2003) and, more recently, in dwarf galaxies (Geha et al. 2013). Despite the huge observational effort made during the last 60 yr, there is still no clear evidence for systematic variations of the IMF and conflicting results have been reported in the past (see Bastian, Covey & Meyer 2010, for a recent review).

Globular clusters (GCs) are in principle among the best places to investigate the distribution of stellar masses at the low-mass end of

★ E-mail: antonio.sollima@oabo.inaf.it

the MF ($0.1 < M/M_{\odot} < 1$). They are composed out of hundreds of thousands to millions of stars, located at the same distance and formed in a short time interval from a chemically relatively homogeneous cloud covering a wide range of masses. Moreover, there is a significant number of GCs at distances <20 kpc for which it is possible to perform a statistically meaningful sampling of their stellar population down to the hydrogen-burning limit with a good level of completeness. On the other hand, the relaxation times of GCs are often smaller than their ages so that the large number of interactions among their stars produces a mass-dependent distribution of kinetic properties (energies and angular momenta). This reflects into the time evolution of the MF, since low-mass stars progressively gain energy, being more prone to evaporation. As mass loss proceeds independently, the MF tends to flatten on time-scales depending on both the internal structure of the cluster and the strength of the external tidal field (Baumgardt & Makino 2003 ; Lamers, Baumgardt & Gieles 2013). Moreover, the tendency towards energy equipartition leads to a radial segregation of different mass groups with the most massive stars moving on less energetic orbits preferentially confined to the innermost cluster regions, while low-mass stars diffuse into an extended halo. For all these reasons, the present-day MF measured in a particular region of a GC neither reflects its IMF nor its global MF. The derivation of the present-day global MF is however still possible by correcting the locally estimated MF by the mass-segregation effects predicted by some suitable dynamical model (see e.g. McClure et al. 1986; Paust et al. 2010). Such corrections depend on the cluster concentration, MF and distance from the cluster centre, but they appear to be generally small close to the half-mass radius (Baumgardt & Makino 2003). So, an alternative approach is to estimate the MF in this region of the cluster and assume it as a good representation of the global MF (e.g. Piotto & Zoccali 1999). On the theoretical side, many surveys of *N*-body simulations have been performed to investigate the evolution of the MF in GC-like objects (Vesperini & Heggie 1997; Baumgardt & Makino 2003; Lamers, Baumgardt & Gieles 2013; Webb & Vesperini 2016). In particular, Leigh et al. (2012) used a set of *N*-body runs assuming different masses, concentrations, orbital eccentricities and tidal environments to reproduce the MFs of a sample of 27 Galactic GCs and showed that the natural evolution of a universal IMF could actually produce the observed cluster-to-cluster differences.

Observationally, since the early 1980s many studies focused on the determination of the MF in individual GCs (without correcting for incompleteness, e.g. Da Costa 1982; Richer et al. 1990; Santiago, Elson & Gilmore 1996; Chabrier & Mera 1997; Paresce & De Marchi 2000; Pulone et al. 2003; Paust, Wilson & van Belle 2014). The first comprehensive studies of the MFs in a number of GCs large enough to explore possible correlations with various cluster parameters have been those by Capaccioli, Piotto & Stiavelli (1993) and Djorgovski, Piotto & Capaccioli (1993), who collected the MFs measured by different authors for a sample of 17 Galactic GCs and reported a dependence of their slopes (measured using stars with masses $m > 0.5\,M_{\odot}$) with the cluster position in the Galaxy. Piotto & Zoccali (1999) analysed in a homogeneous way deep *Hubble Space Telescope* (*HST*) images taken near the half-mass radii of seven GCs reaching a limiting mass of $m \sim 0.3\,M_{\odot}$. They found that the MF slopes correlate with the orbital destruction rates of the clusters in the Galaxy and anticorrelate with their half-mass relaxation times although their small sample hampered any firm conclusion on the significance of these correlations. De Marchi, Paresce & Pulone (2007), used a sample of *HST* and Very Large Telescope (VLT) data for a sample of 20 GCs and found a well-defined correlation between the slope of their MFs and their King model concentration parameter *c*. Finally, Paust et al. (2010) derived the central and global present-day MFs of 17 GCs as part of the Advanced Camera for Surveys (ACS) Galactic Globular Clusters treasury project (Sarajedini et al. 2007) by comparing ACS/*HST* photometric data with multimass dynamical models. They found a significant correlation between the MF slope and the central density (or equivalently the central surface brightness), while detecting only marginal statistical significance of the previously reported correlations with other parameters.

In this paper, we use the ACS treasury project data base to extend the census of GC MFs to a sample of 35 clusters, more than doubling the sample already analysed by Paust et al. (2010). By means of a comparison with multimass analytical models we derive the global MFs of the analysed clusters and investigate possible correlations with their structural and dynamical parameters. In Section 2, we present the data base used in this work. The adopted dynamical models are described in Section 3. Section 4 is devoted to the description of the algorithm adopted to determine global MFs and other structural parameters. The obtained MFs and the analysis of their shapes are presented in Section 5. In Section 6, we search for correlations with various cluster parameters. We finally discuss our results in Section 7.

2 OBSERVATIONAL MATERIAL

The derivation of the global MFs and the cluster parameters has been performed through the analysis of three different kinds of data sets: photometry, surface brightness profiles and individual stellar radial velocities.

The photometric data consist of high-resolution *HST* observations of a sample of 66 Galactic GCs obtained as part of the *Globular Cluster ACS Treasury Project* (Sarajedini et al. 2007). The data have been obtained using deep images obtained with the ACS Wide Field Channel through the F606W and F814W filters. The field of view of the camera (202 arcsec × 202 arcsec) was centred on the cluster centres with a dithering pattern to cover the gap between the two chips, allowing a full coverage of the core of all the GCs considered in our analysis. This survey provides deep colour–magnitude diagrams (CMDs) providing photometry of main-sequence (MS) stars down to the hydrogen-burning limit (at $M_V \sim 10.7$) with a signal-to-noise ratio S/N > 10 for all target clusters. The results of artificial star experiments are also available to allow an accurate estimate of the completeness level and photometric errors. A detailed description of the photometric reduction, astrometry and artificial star experiments can be found in Anderson et al. (2008). Within this data base, we excluded from our analysis all GCs with (i) evidence of large ($\Delta Y > 0.1$) helium variation (ω Cen, NGC 2808, NGC 6388 and NGC 6441), (ii) significant contamination by either bulge (NGC 6624 and NGC 6637) or Sagittarius dwarf galaxy stars (M54), or (iii) a completeness level estimated in the innermost arcminute at the hydrogen-burning limit smaller than $\psi < 10$ per cent. Thirty-five GCs passed the above selection criteria (see Table 1).

The surface brightness profiles for most GCs of our sample were taken from Trager, King & Djorgovski (1995). They were constructed from generally inhomogeneous data based mainly on the Berkeley Globular Cluster Survey (Djorgovski & King 1984). The surface brightness profile of each cluster has been derived by matching several sets of data obtained with different techniques (aperture photometry on CCD images and photographic plates, photoelectric observations, star counts, etc.). Moreover, the profiles of the more

Table 1. Parameters of the best-fitting models.

NGC	α	$\log(M_{\rm lum}/{\rm M}_\odot)$	$\log(M_{\rm dyn}/{\rm M}_\odot)$	$r_{\rm h}$ (pc)	$f_{\rm remn}$	$\log(t_{\rm rh}/{\rm yr})$	$M_{\rm dyn}/L_{\rm V}$ $({\rm M}_\odot/{\rm L}_\odot)$	$\log\rho_0$ $({\rm M}_\odot/{\rm pc}^3)$	$\log\rho_{\rm h}$ $({\rm M}_\odot/{\rm pc}^3)$
288	−0.66 ± 0.04	4.67 ± 0.04	4.96 ± 0.03	9.12	0.50 ± 0.05	9.60	1.89 ± 0.49	1.92	1.16
1261	−0.65 ± 0.03	4.93 ± 0.10	5.23 ± 0.05	5.70	0.50 ± 0.11	9.39	1.51 ± 0.53	3.26	2.04
1851	−0.69 ± 0.03	5.14 ± 0.07	5.51 ± 0.04	5.14	0.57 ± 0.08	9.43	1.64 ± 0.49	4.49	2.45
2298	0.11 ± 0.03	4.18 ± 0.12		3.19					
3201	−1.26 ± 0.09	4.81 ± 0.03	5.08 ± 0.03	6.41	0.47 ± 0.05	9.46	1.95 ± 0.50	3.05	1.74
4147	0.03 ± 0.05	4.21 ± 0.13	4.81 ± 0.22	5.22	0.75 ± 0.26	9.12	2.13 ± 1.36	3.83	1.73
4590	−1.27 ± 0.07	4.87 ± 0.06	5.29 ± 0.06	8.60	0.62 ± 0.09	9.74	2.91 ± 0.89	3.12	1.56
4833	−0.69 ± 0.08	5.10 ± 0.03	5.35 ± 0.07	8.60	0.43 ± 0.08	9.71	1.32 ± 0.39	3.21	1.62
5024	−1.41 ± 0.11	5.53 ± 0.05	5.82 ± 0.06	15.12	0.49 ± 0.08	10.34	1.95 ± 0.56	3.09	1.36
5053	−1.29 ± 0.03	4.62 ± 0.03	4.78 ± 0.11	19.30	0.32 ± 0.11	10.11	1.64 ± 0.57	0.59	0.00
5272	−0.95 ± 0.08	5.35 ± 0.05	5.61 ± 0.04	7.29	0.45 ± 0.07	9.73	1.68 ± 0.46	3.76	2.10
5286	−0.61 ± 0.03	5.29 ± 0.07	5.71 ± 0.08	4.43	0.61 ± 0.11	9.43	1.30 ± 0.45	4.28	2.85
5466	−1.68 ± 0.09	4.82 ± 0.03	4.77 ± 0.11	24.64	−0.12 ± 0.12	10.25	1.25 ± 0.45	0.98	−0.33
5904	−0.88 ± 0.10	5.27 ± 0.04	5.58 ± 0.04	7.66	0.51 ± 0.06	9.73	1.99 ± 0.53	3.86	2.00
5986	−0.65 ± 0.07	5.20 ± 0.07	5.48 ± 0.05	5.47	0.48 ± 0.09	9.46	1.43 ± 0.44	3.53	2.34
6093	−0.14 ± 0.04	5.10 ± 0.08	5.58 ± 0.07	3.39	0.67 ± 0.11	9.16	1.54 ± 0.52	4.97	3.07
6101	−1.60 ± 0.15	5.11 ± 0.03		18.75					
6144	−0.15 ± 0.06	4.42 ± 0.06		5.82					
6205	−0.60 ± 0.08	5.34 ± 0.04	5.77 ± 0.03	6.87	0.63 ± 0.06	9.71	2.01 ± 0.53	3.43	2.34
6218	−0.32 ± 0.04	4.60 ± 0.06	4.95 ± 0.03	4.09	0.55 ± 0.06	9.01	1.50 ± 0.41	3.38	2.19
6254	−0.48 ± 0.09	4.94 ± 0.05	5.33 ± 0.05	5.21	0.59 ± 0.07	9.34	1.93 ± 0.55	3.79	2.26
6304	−1.89 ± 0.19	5.17 ± 0.05	5.27 ± 0.05	5.69	0.20 ± 0.07	9.57	3.05 ± 0.86	4.13	2.08
6341	−0.75 ± 0.05	5.15 ± 0.06	5.48 ± 0.03	5.39	0.53 ± 0.07	9.47	1.56 ± 0.44	4.47	2.36
6397	−0.40 ± 0.03	4.61 ± 0.02	4.96 ± 0.02	4.60	0.56 ± 0.03	9.14	1.09 ± 0.26	5.65	2.05
6541	−0.49 ± 0.05	5.09 ± 0.06	5.41 ± 0.05	4.64	0.53 ± 0.08	9.32	1.64 ± 0.49	4.85	2.49
6584	−0.53 ± 0.02	4.62 ± 0.13		4.67					
6656	−0.98 ± 0.13	5.42 ± 0.02	5.69 ± 0.03	6.25	0.46 ± 0.04	9.70	1.86 ± 0.46	3.88	2.38
6723	−0.24 ± 0.05	4.84 ± 0.07	5.23 ± 0.11	5.04	0.59 ± 0.13	9.28	1.91 ± 0.71	3.37	2.20
6752	−0.49 ± 0.07	4.97 ± 0.03	5.38 ± 0.02	5.68	0.60 ± 0.04	9.44	1.94 ± 0.48	5.03	2.19
6779	−0.55 ± 0.03	4.79 ± 0.09		4.92					
6809	−0.89 ± 0.05	4.90 ± 0.03	5.29 ± 0.03	6.31	0.59 ± 0.04	9.50	1.83 ± 0.45	2.81	1.97
6934	−0.77 ± 0.04	4.84 ± 0.10		5.98					
7078	−1.16 ± 0.07	5.54 ± 0.05	5.81 ± 0.03	7.71	0.47 ± 0.06	9.89	1.79 ± 0.48	4.16	2.23
7089	−0.83 ± 0.07	5.53 ± 0.05	5.89 ± 0.06	7.87	0.56 ± 0.08	9.88	1.98 ± 0.57	4.11	2.28
7099	−0.72 ± 0.02	4.82 ± 0.07	5.16 ± 0.05	5.53	0.54 ± 0.08	9.37	1.48 ± 0.44	5.04	2.01

distant and/or faint GCs are often noisy and do not extend beyond a few core radii. For this reason we adopted, where available, the number density profiles calculated by Miocchi et al. (2013) from wide-field photometry. Finally, the density profile calculated by Melbourne et al. (2000) and Alonso-García et al. (2012) have been adopted for NGC 4833 and NGC 6144, respectively. Because of the better angular resolution of *HST* data, ACS observations sample the innermost portion of our clusters much more accurately than any other previous ground-based analysis. For this reason, the surface brightness profile of the innermost 1.6 arcmin has been calculated directly from ACS data by summing completeness-corrected F606W fluxes

$$\mu = -2.5\log\left(\sum_i \frac{10^{-0.4\,{\rm F606W}_i}}{c_i}\right)$$

in annuli of 0.1 arcmin width and matched to the adopted external profile using the overlap region. The completeness factors c_i have been calculated for all stars as the fraction of recovered objects[1] in the artificial star catalogue among all stars within 0.05 arcmin from the position of each individual star and within 0.25 mag of the F606W and F814W magnitudes of each individual star.

Among the 35 GCs of our sample, we found large sets (>50) of available radial velocities in the literature for 29 of them (see table A1 of Baumgardt 2017 for the references for each cluster). Radial velocities from different sources were corrected for systematic shifts using the stars in common. Additional radial velocities for clusters NGC 1261, NGC 5986, NGC 6304 and NGC 6541 were derived from archival FLAMES@VLT spectra collected under the observing programmes 193.D-0232 (PI: Ferraro) and 093.D-0628 (PI: Zocchi). For this task, pipeline-reduced spectra were cross-correlated with the solar spectrum observed with the same setups as the science observations using the task *fxcor* within the IRAF package.[2]

3 MODELS

As explained in Section 1, in dynamically evolved stellar systems like GCs, the distribution of stars depends on their mass. Hence,

[1] An artificial star has been considered recovered if its input and output magnitudes differ by less than 2.5 log(2) (∼0.75) mag in both F606W and F814W magnitudes.

[2] IRAF is distributed by the National Optical Astronomy Observatories, which are operated by the Association of Universities for Research in Astronomy, Inc., under cooperative agreement with the National Science Foundation.

in order to derive the global MF of our target clusters, their MFs measured in the ACS field of view need to be corrected using the prescriptions of a dynamical model. The structure and kinematics of our clusters have been modelled with a set of isotropic multi-mass King–Michie models (Gunn & Griffin 1979). According to this model, the distribution function is given by the sum of the contribution of several mass groups

$$f(E,L) = \sum_{j=1}^{H} k_j \left[\exp\left(-\frac{A_j E}{\sigma_{\rm K}^2} \right) - 1 \right]$$

$$\sum_{j=1}^{H} f_j(m_j, r, v) = \sum_{i=1}^{H} k_j \left[\exp\left(-\frac{A_j(v^2 + 2\psi)}{2\sigma_{\rm K}^2} \right) - 1 \right] \quad (1)$$

where E is the energy per unit mass, m_j is the mass of the stars in the jth component, H is the number of mass components, k_j are coefficients determining the relative fraction of stars in the jth mass group, $\sigma_{\rm K}^2$ is an energy normalization constant, r and v are the 3D distance from the cluster centre and velocity and A_i are coefficients governing the kinetic energy balance among different mass groups. In the original formulation by Gunn & Griffin (1979), $A_j \propto m_j$. Although this last assumption is arbitrary, it has been shown that it reproduces the structure and the degree of mass segregation of both N-body simulations during most of their evolution and real GCs (Sollima et al. 2015, 2017). In principle, a degree of radial anisotropy can be included by multiplying the distribution function of equation (1) by a term dependent on the angular momentum. However, because of the lack of accurate proper motion determinations for the GCs analysed here, no stringent constraints on the degree of anisotropy can be put. Moreover, the recent analysis by Watkins et al. (2015) based on accurate *HST* proper motions in 22 Galactic GCs showed that they appear to be isotropic across the field of view analysed by these authors. For the above reasons, we prefer to consider only isotropic models to limit the number of free parameters. We adopted 23 mass groups: 8 evenly spaced bins comprised between 0.1 $M_\odot$ and the mass at the tip of the red giant branch (RGB, $M_{\rm tip}$) and 15 evenly spaced bins between $M_{\rm tip}$ and 2.6 $M_\odot$ (i.e. the largest mass allowed in our synthetic population; see Section 4).

The distribution function in equation (1) can be integrated over the velocity domain to obtain the 3D density and velocity dispersion of each mass group.

$$\nu_j(r) = \int_0^{\sqrt{-2\psi(r)}} 4\pi v^2 k_j f_j(v, r, m_j) dv$$

$$\sigma_{v,j}^2(r) = \frac{\int_0^{\sqrt{-2\psi(r)}} 4\pi k_j v^4 f_j(v, r, m_j) dv}{\nu_j(r)} \quad (2)$$

while the potential at any radius is determined by the Poisson equation

$$\nabla^2 \psi = 4\pi G \rho \quad (3)$$

where

$$\rho(r) = \sum_{j=1}^{H} m_j \nu_j(r)$$

equations (1)–(3) have been integrated after assuming, as a boundary condition, a value of the potential and its derivative at the centre (ψ_0; $d\psi/dr(0) = 0$) outward till the radius $r_{\rm t}$ at which both density and potential vanish.

Observational quantities (global MF, surface brightness and line-of-sight velocity dispersion profiles) can be obtained through the relations

$$N_j = 4\pi \int_0^{r_{\rm t}} r^2 \nu_j dr$$

$$\mu(R) = -2.5 \log \left(\sum_{j=1}^{H} \Gamma_j \Upsilon_j \right)$$

$$\sigma_{{\rm LOS},j}^2(R) = \frac{2}{3\Gamma_j(R)} \int_R^{r_t} \frac{\nu_j \sigma_{v,j}^2 r}{\sqrt{r^2 - R^2}} dr \quad (4)$$

where

$$\Gamma_j(R) = 2 \int_R^{r_t} \frac{\nu_j r}{\sqrt{r^2 - R^2}} dr$$

is the projected number density and Υ_j is the average V-band flux of stars in the jth component.

These models are completely defined by the free parameters $W_0 \equiv -\psi_0/\sigma_{\rm K}^2$, k_j (unequivocally defining the shape of all profiles), $r_{\rm c} \equiv \sqrt{9\sigma_{\rm K}^2/4\pi G\rho(0)}$ (defining the size of the model) and $\sigma_{\rm K}^2$ (determining the normalization in mass and velocity dispersion). The total mass and luminosity of the model can finally be calculated as

$$M = \sum_{j=1}^{H} N_j m_j$$

$$L_{\rm V} = \sum_{j=1}^{H} N_j \Upsilon_j$$

4 METHOD

The algorithm adopted to determine the global MF of each GC is similar to that described in Sollima, Bellazzini & Lee (2012) and Sollima et al. (2017) and can be schematically described as follows:

(i) As a first step, a synthetic stellar population has been constructed by randomly extracting $N = 10^6$ stars from a Kroupa (2001) IMF between 0.1 and 8 $M_\odot$. A fraction $f_{\rm b}$ of binaries has also been simulated by randomly pairing $N_{\rm b} = 2Nf_{\rm b}$ synthetic stars. All single stars and stars in binaries with masses $m > M_{\rm tip}$ have been turned into compact remnants following the prescription

$m_{\rm WD} = 0.109\, m + 0.428$ (Kalirai et al. 2009)

Due to the adopted upper limit of the IMF, only white dwarfs are created in this process. This is consistent with the assumption that all neutron stars and black holes are ejected in the early stage of cluster evolution because of the effect of natal kicks and/or *Spitzer* instability (Kruijssen 2009).

(ii) The corresponding synthetic CMD has been constructed by interpolating the masses of visible stars with the mass–luminosity relation of a suitable isochrone from the Dotter et al. (2007) data base. For each cluster, the isochrone metallicity, age and α-enhancement as well as the reddening and distance modulus listed in Dotter et al. (2010), providing an excellent fit to the ACS data, have been adopted A synthetic horizontal branch (HB) has been simulated for each cluster using the tracks by Dotter et al. (2007), tuning the mean mass and mass dispersion along the HB to reproduce the observed HB morphology. The magnitude and colours of binary systems have been calculated by summing the fluxes of the two components in both passbands. We do not account for the negligible contamination of fore/background Galactic field interlopers possibly present in the ACS field of view. Indeed, the Galactic model of Robin et al. (2003) predicts <50 field stars, corresponding to a

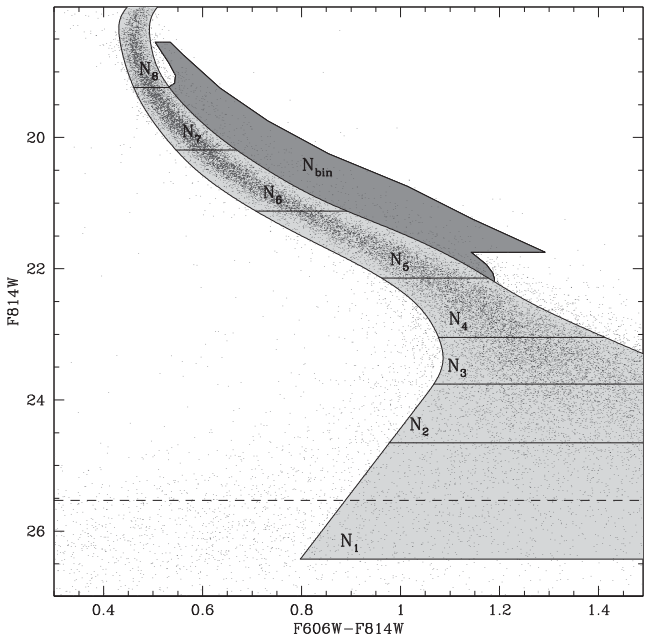

Figure 1. Selection boxes adopted for the population of single stars (m_1–m_8) and binaries (bin) of NGC 288. The observed CMD is overplotted. The 50 per cent completeness limit is marked by the dashed line.

fraction <0.1 per cent, contained in the selection box (see below) and within the innermost 1.6 arcmin even in the low-latitude GCs of our sample;

(iii) The synthetic stars (singles, binaries and remnants) have been binned in mass (see Section 3) and for each bin a fraction $1 - X_j$ of particles has been randomly rejected. The average F606W fluxes (Υ_j) of the remaining stars in each mass group have also been calculated;

(iv) A dynamical model is constructed tuning the parameters W_0 and r_c in order to obtain the best fit of the surface brightness profile and the k_j coefficients are modified to reproduce the MF of the mock catalogue (see equation 4);

(v) The distribution in phase space (3D position and velocity) of synthetic stars was then extracted from the modelled distribution function using the von Neumann rejection technique: for each star, a random position in phase space (r, v) is extracted and assigned to the star only if a random number between 0 and 1 turns out to be smaller than $f(m_i, r, v)/f(m_i, 0, 0)$. Projected distance and LOS velocities have then been calculated assuming an isotropic distribution;

(vi) For each synthetic star, a particle from the artificial star catalogue with distance from the cluster centre within 0.05 arcmin and magnitudes within 0.25 mag with respect to the same quantities of the given star, has been extracted and, if recovered, the magnitude and colour shift with respect to its input quantities have been added to those of the corresponding star. In this way, a mock CMD accounting for photometric errors and incompleteness has been obtained;

(vii) The number of stars within 1.6 arcmin from the cluster centre (i.e. the extent of the ACS field of view) and contained in nine regions of both the observed and the mock CMD have been counted (see Fig. 1). In particular, we defined

(a) eight F606W magnitude intervals corresponding to the first eight mass intervals and including all stars with colours within three times the photometric error corresponding to their magnitudes;

(b) a region including the bulk of the binary population with high-mass ratios ($q > 0.5$). This last region is delimited in magnitude by the loci of binaries with primary star mass $m_1 = 0.45\,M_\odot$ (faint boundary) and $m_1 = 0.75 M_\odot$ (bright boundary), and in colour by the MS ridge line (blue boundary) and the equal-mass binary sequence (red boundary), both redshifted by three times the photometric error.

(viii) The retention fractions (X_j) of stars in the eight mass bins and the global binary fraction f_b are adjusted by multiplying them for corrective terms which are proportional to the ratio between the relative number counts in each bin of the observed sample and the corresponding model prediction

$$X'_j = X_j \left(\frac{Q_j^{obs} Q_8^{mock}}{Q_8^{obs} Q_j^{mock}} \right)^{\eta}$$

$$f'_b = f_b \left(\frac{Q_{bin}^{obs}}{Q_{bin}^{mock}} \frac{\sum_{j=1}^{8} Q_j^{mock}}{\sum_{j=1}^{8} Q_j^{obs}} \right)^{\eta}$$

where Q_j and Q_{bin} are the number of stars observed in the jth single and in the binary selection boxes, respectively, the superscripts obs and mock indicate counts measured either in the observed or in the mock catalogues, respectively, and η is a softening parameter, set to 0.5, used to avoid divergence. All the coefficients X_j with $j > 8$ have been set equal to 1.

Steps from (iii) to (viii) have been repeated until convengerce.

For the first step, we adopted $X_j = 1$ for all j and $f_b = 5$ per cent. The above-described procedure converged after ∼20 iterations for all the considered clusters. The global MF of single stars can therefore be calculated directly from the mock catalogue simulated in the last iteration.

A final step is constituted by the mass normalization of the model. This can be done by best-fitting two independent quantities: (i) the actual number of stars in the observed (Q^{obs}) and in the mock (Q^{mock}) CMDs, and (ii) the amplitude of the velocity dispersion profile. The former way allows us to estimate the mass in luminous stars as

$$M_{lum} = \frac{Q^{obs}}{Q^{mock}} \sum_{i=1}^{N_{sin}+N_{bin}} m_i$$

where the sum is extended to all single and binary stars in the final mock catalogue excluding remnants. For clusters with available radial velocities, the latter way provides an estimate of the dynamical mass (M_{dyn}). The best-fitting value of M_{dyn} has been chosen as the one minimizing the penalty function

$$\mathcal{L} = \sum_{i=1}^{N} \left(\frac{(v_i - \overline{v})^2}{\sigma^2_{LOS,8}(R_i) + \epsilon_i^2} + \ln(\sigma^2_{LOS,8}(R_i) + \epsilon_i^2) \right)$$

where v_i is the radial velocity of the ith star, $\overline{v}$ is the systemic velocity of the cluster, ϵ_i is the individual uncertainty on the radial velocity and $\sigma_{LOS,8}(R_i)$ is the line-of-sight velocity dispersion predicted by the best-fitting model at the projected distance R_i of the ith star for the eighth mass group. The choice of the eighth mass bin is because radial velocities are available only for stars along the RGB which cover a restricted range of masses. Because of the dependence of kinematics on mass, it is therefore necessary to compare the observed velocity dispersion profile with that of the corresponding mass bin to avoid bias in the mass estimate.

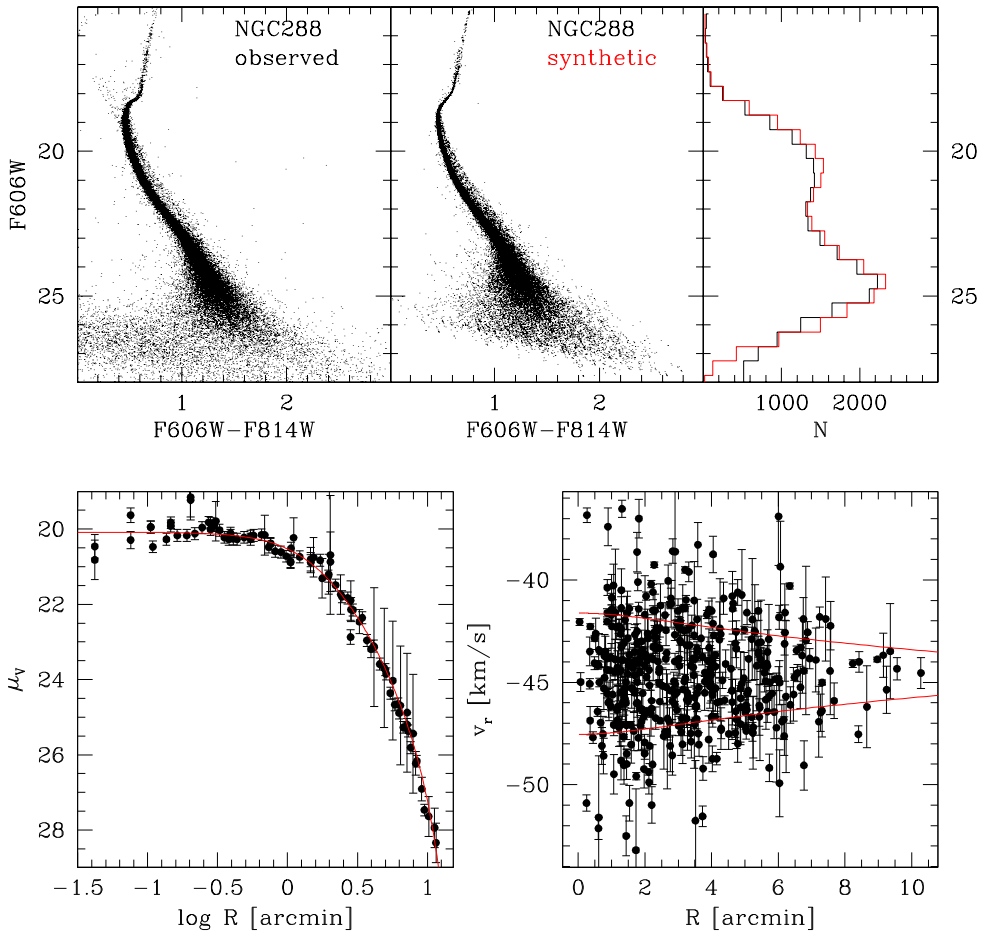

Figure 2. Comparison between three observables of NGC 288 and the corresponding model prediction (red lines; grey in the printed version of the paper). Bottom-left panels: surface brightness profile; bottom-right panel: velocity dispersion profile; upper-left panels: CMDs and upper-right panels: F606W luminosity function. The predicted $\pm\sigma_{\rm LOS}$ range is indicated in the bottom-right panel.

Once luminous and dynamical masses are determined the fraction of dark mass can be calculated as

$$f_{\rm remn} = 1 - \frac{M_{\rm lum}}{M_{\rm dyn}}$$

Finally, the central density ρ_0, the half-mass radius $r_{\rm h}$, the $M_{\rm dyn}/L_{\rm V}$ ratio of the best-fitting model are computed as well as the half-mass relaxation time as

$$t_{\rm rh} = 0.138 \frac{M_{\rm dyn}^{1/2} r_{\rm h}^{3/2}}{G^{1/2} \overline{m} \ln(\gamma M_{\rm dyn}/\overline{m})} \quad \text{(Spitzer 1987)} \qquad (5)$$

with $\gamma = 0.11$ (Giersz & Heggie 1996). The outcome of the application of the above the technique for NGC 288 is shown in Fig. 2, as an example.

5 RESULTS

The global MFs of the 35 GCs analysed in this work are shown in Figs 3–7 and the derived dynamical parameters are listed in Table 1. Among the various parameters, the power-law index α of the MF has been calculated for stars more massive than 0.2 $M_\odot$, since stars below this limit often show relatively low levels of completeness ($\psi < 50$ per cent) and their relative fraction is subject to large errors. For testing purpose, we also calculate α adopting a high-mass cut at $m > 0.3\,M_\odot$. In the scale adopted here, a Salpeter (1955) MF

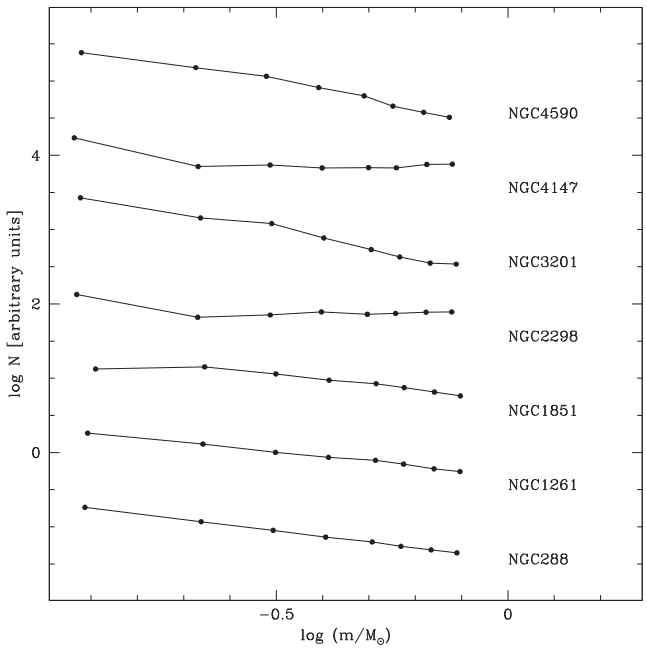

Figure 3. Global MFs of NGC 288, NGC 1261, NGC 1851, NGC 2298, NGC 3201, NGC 4147 and NGC 4590. An arbitrary shift has been added to each MF for clarity.

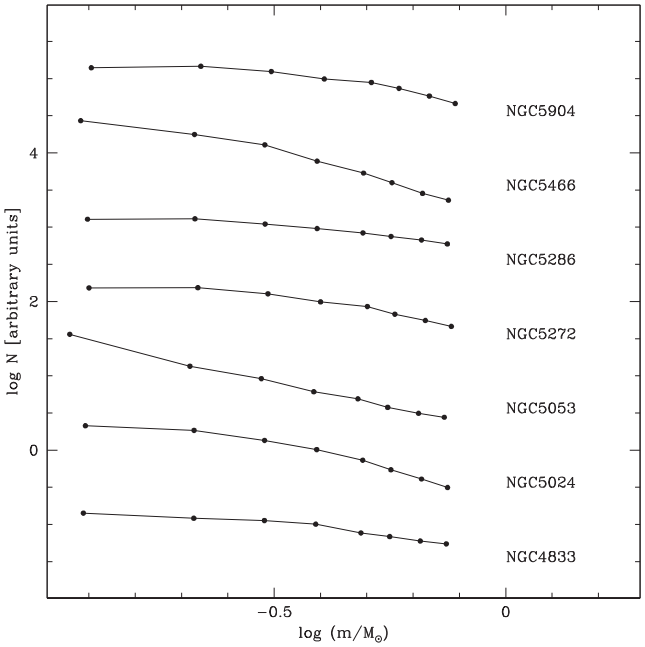

Figure 4. Same as Fig. 3, but for NGC 4833, NGC 5024, NGC 5053, NGC 5272, NGC 5286, NGC 5466 and NGC 5904.

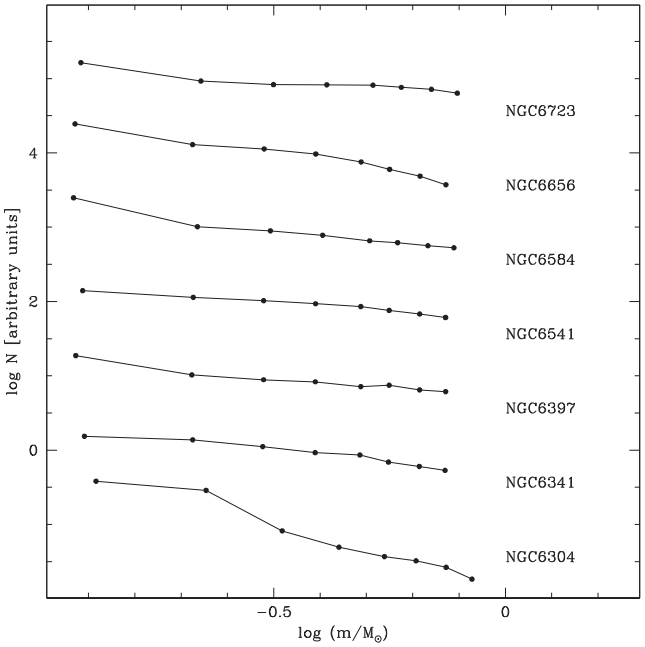

Figure 6. Same as Fig. 3, but for NGC 6304, NGC 6341, NGC 6397, NGC 6541, NGC 6584, NGC 6656 and NGC 6723.

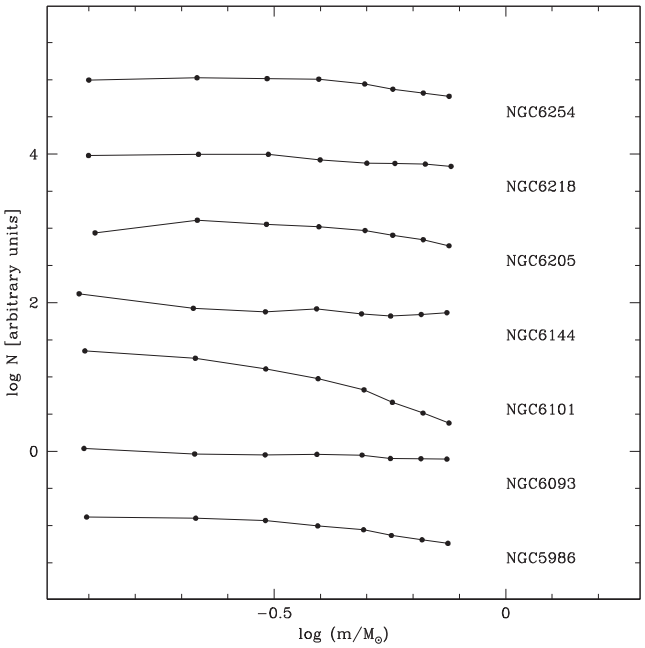

Figure 5. Same as Fig. 3 but for NGC 5986, NGC 6093, NGC 6101, NGC 6144, NGC 6205, NGC 6218 and NGC 6254.

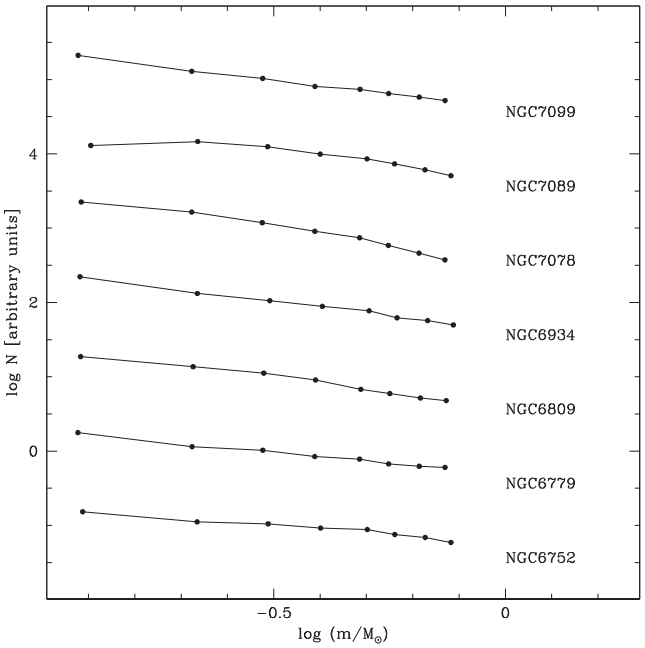

Figure 7. Same as Fig. 3, but for NGC 6752, NGC 6779, NGC 6809, NGC 6934, NGC 7078, NGC 7089 and NGC 7099.

has $\alpha = -2.35$ and a Kroupa (2001) MF would have a best-fitting slope of $\alpha \sim -1.64$.

The estimated slopes cover a wide range from $\alpha = -1.89$ (NGC 6304) to 0.11 (NGC 2298). Thirteen GCs are in common with the work by Paust et al. (2010), who estimated MFs using the same photometric data set and also used multimass dynamical models. We show the comparison between the two works in Fig. 8. The mean difference between the two studies is $\Delta\alpha$(this work − Paust) $= 0.16 \pm 0.13$ consistent with only a small (if any) systematic shift. However, the dispersion about the mean ($\sigma = 0.47$) is not compatible with the combined errors of the two works. In this context, it should be noted that the formal error quoted by Paust et al. (2010) as well as those listed in Table 1 are errors on the MF fit and do not reflect the actual error budget (due to incomplete radial sampling, errors of the estimated completeness factor, isochrone/dynamical model inadequacy, etc.). Given the above considerations, we believe that a more realistic uncertainty of the MF slopes of both works is of the order of $\sigma_\alpha \sim 0.3$. It is worth noting that for NGC 6093, the difference between the two estimates exceeds $\Delta\alpha > 1.2$. Moreover, for NGC 5466, we find an unphysical

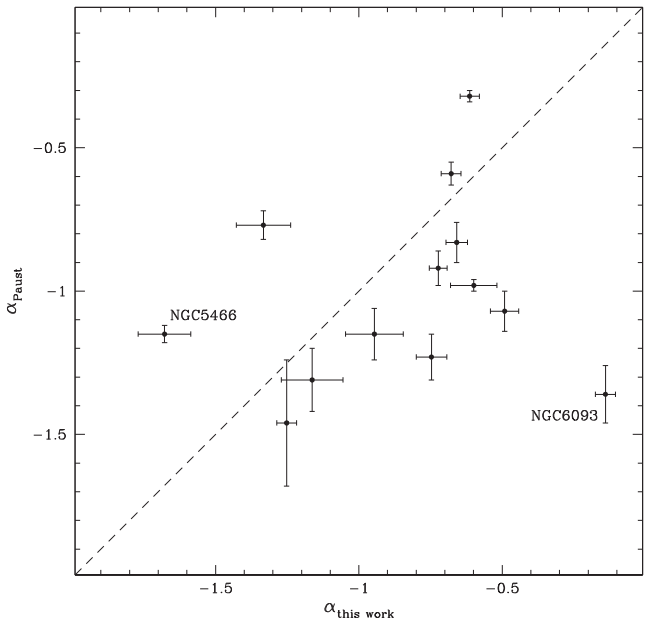

Figure 8. Comparison between the MF slopes derived in this work and those determined by Paust et al. (2010) for the 13 GCs in common. The one-to-one relation is marked by the dashed line. The location of NGC5466 and NGC6093 is shown.

solution with $M_{\rm lum} > M_{\rm dyn}$. Among the GCs in common, these are those with the smallest fraction of stars contained within the ACS field of view. In this situation, even a small difference in the fitting process can produce large extrapolation errors. For comparison, a similar analysis of NGC 5466 performed in Sollima et al. (2017) using MF constraints in the outer portion of this cluster leads to a significantly flatter MF slope ($\alpha = -0.97$). The mean difference between the MF slopes derived adopting different low-mass cuts is $\Delta\alpha_{0.3-0.2} = -0.05 \pm 0.01$, indicating only a small dependence of the estimated MF slopes on the adopted lower mass limit.

An inspection of the MFs reveals that while some of them are well fitted by single power laws, others show strong deviations from a power-law MF. To investigate this issue further, we correlated the χ^2 value of the power law fitted with various cluster parameters. A single significant correlation has been found with the MF slope itself, in the sense that flatter MFs present better power-law fits. To highlight this result, we plot in Fig. 9, the residuals of the power-law fit for clusters with $\alpha \gtrless -1$. It is apparent that while clusters with a relatively flat MF ($\alpha > -1$) show no significant deviation from the best-fitting power law, clusters with steep MFs have a convex shape. In particular, a point of maximum curvature is apparent at $\log(m/{\rm M}_\odot) \sim -0.4$ (corresponding to a mass $m \sim 0.4\,{\rm M}_\odot$). The same evidence remains apparent even using the α values calculated adopting a high-mass cut at $m > 0.3\,{\rm M}_\odot$, indicating a negligible effect of the uncertainties of the MF estimate at very low masses.

6 ANALYSIS OF CORRELATIONS

The MF slopes derived here constitute the largest available data base and can be therefore used to search for correlations with other structural and general parameters. We considered the following parameters to look for possible correlations with the MF slope: Position in the Galaxy ($R_{\rm GC}$, Z from the Harris catalogue; Harris 1996, 2010 edition), destruction rates (ν; from Allen, Moreno & Pichardo 2006, 2008), concentration (c; from McLaughlin & van der Marel 2005), age and metallicity (t_9, [Fe/H]; from Dotter et al. 2010), central V-band surface brightness, mass-to-light (M/L) ratio, central and half-mass density, half-mass relaxation time and remnant mass fraction ($\mu_{\rm V,0}$, $M_{\rm dyn}/L_{\rm V}$, ρ_0, $\rho_{\rm h}$, $t_{\rm rh}$, $f_{\rm remn}$; from the best-fitting multimass model adopted in this analysis).

As a first step, we analysed univariate correlations between α and the other parameters. For this purpose, a Monte Carlo procedure has been applied to estimate the significance of the obtained correlations. For each of the considered parameters, we performed an error-weighted least-squares fit and calculated the χ^2 values. Then, the same analysis has been performed on 1000 realizations simulated by randomly swapping the values of the independent variable among the GCs of the sample. The probability that the observed correlation is significant is therefore given by the fraction of realizations with a χ^2 larger than the observed value. From this approach, we found three significant ($P > 99.7$ per cent) correlations with $\log t_{\rm rh}$, $f_{\rm remn}$ and $\log\rho_{\rm h}$, and a marginally significant correlation (95 per cent $< P <$ 99.7 per cent) with the central density, while no significant correlations have been found with other parameters suggested by previous works (see Section 1). The entire

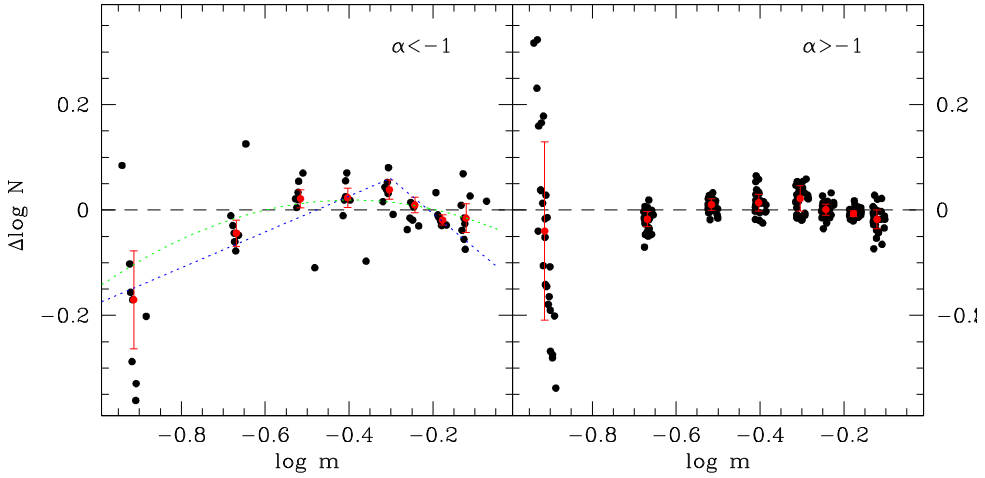

Figure 9. Residuals of the power-law fit for clusters with $\alpha < -1$ (left-hand panel) and $\alpha > -1$ (right-hand panel). The average residuals and their standard deviations for all mass bins are marked with red dots and error bars (grey in the printed version of the paper). The Kroupa (2001; blue line) and Chabrier (2003; green line) IMFs are also marked with dotted lines.

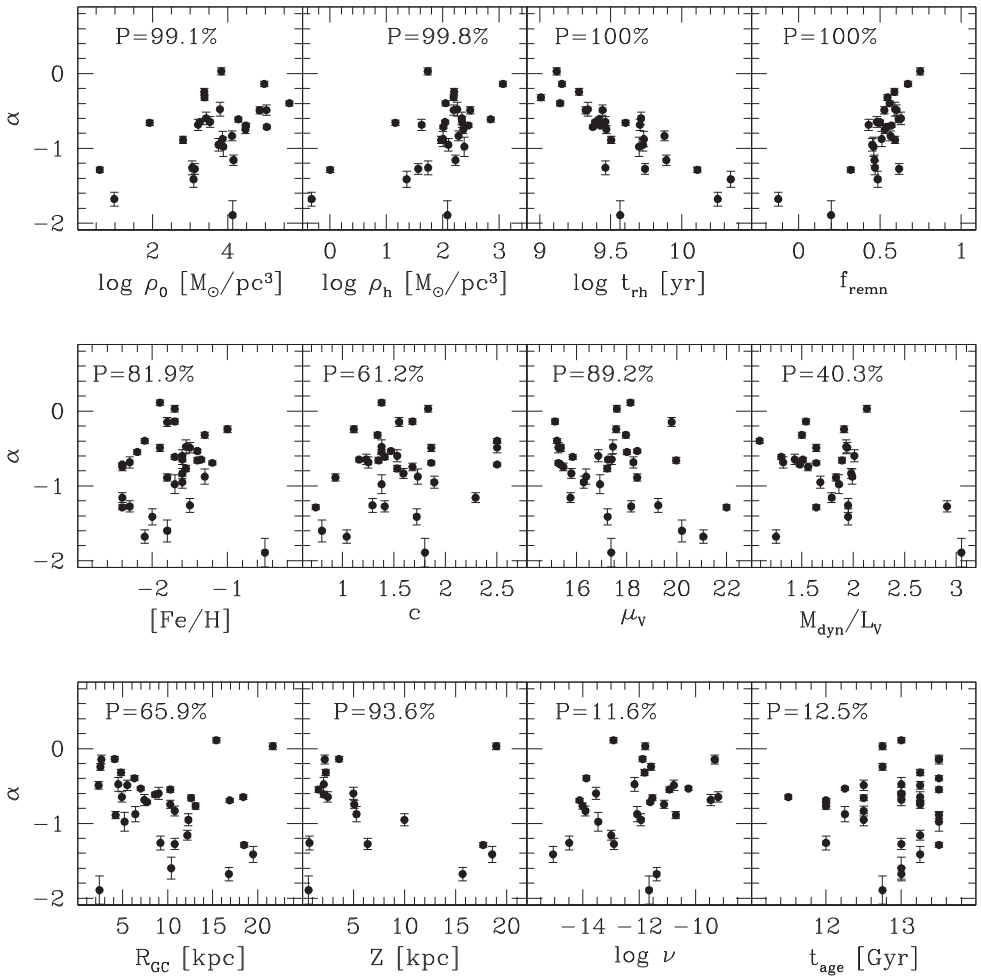

Figure 10. Univariate correlations between the global MF slope α and various parameters. The statistical significance (P) of each correlation is indicated.

set of correlations and their associated probabilities are shown in Fig. 10.

We note that, the correlation between α and logt_{rh} has a surprisingly small dispersion ($\sigma = 0.29$ i.e. compatible with the actual α uncertainties; see Section 5). The only cluster straying from the observed trend is NGC 6304 with an MF slope $\alpha = -1.89 \pm 0.19$ steeper than those of the other GCs of our sample. It should be noted however that this cluster is close to the Galactic bulge whose MF is known to be bottom heavy (Zoccali et al. 2000; Calamida et al. 2015). We therefore cannot exclude the possibility that the peculiar MF measured in this GC is due to a significant contamination from the bulge. Another way to visualize the above correlation is shown in Fig. 11, where the MF slope α is plotted against the ratio of age to present-day half-mass relaxation time t_{age}/t_{rh}. Again, GCs define a very tight correlation in this plot, indicating an evolutionary sequence. In other words, after the same number of present-day half-mass relaxation times clusters have similar MF slopes regardless of their orbits and chemical compositions. Another investigation can be made based on the location of clusters in the t_{age}/t_{rh}–α plane as shown in Fig. 11: while GCs with $t_{age}/t_{rh} < 1$ have MF slopes $\alpha \sim -1.5$ similar to that of a Kroupa (2001) MF, the mean MF slope increases by ∼0.5 dex at $t_{age}/t_{rh} \sim 3$.

We also extended our analysis to bivariate correlations. The χ^2 of a bilinear fit of all the possible pairs of parameters has been calculated and compared. The smallest χ^2 are all those found by assuming

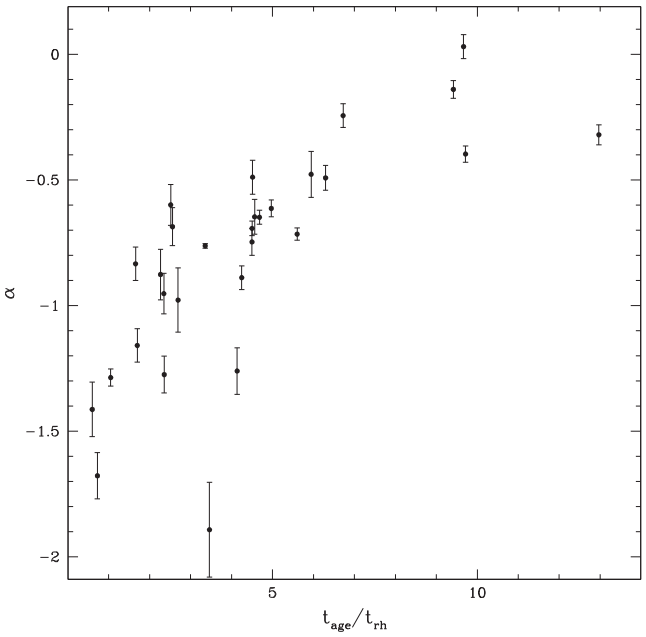

Figure 11. MF slope α as a function of the ratio between cluster age and present-day half-mass relaxation time for the 29 GCs of our sample.

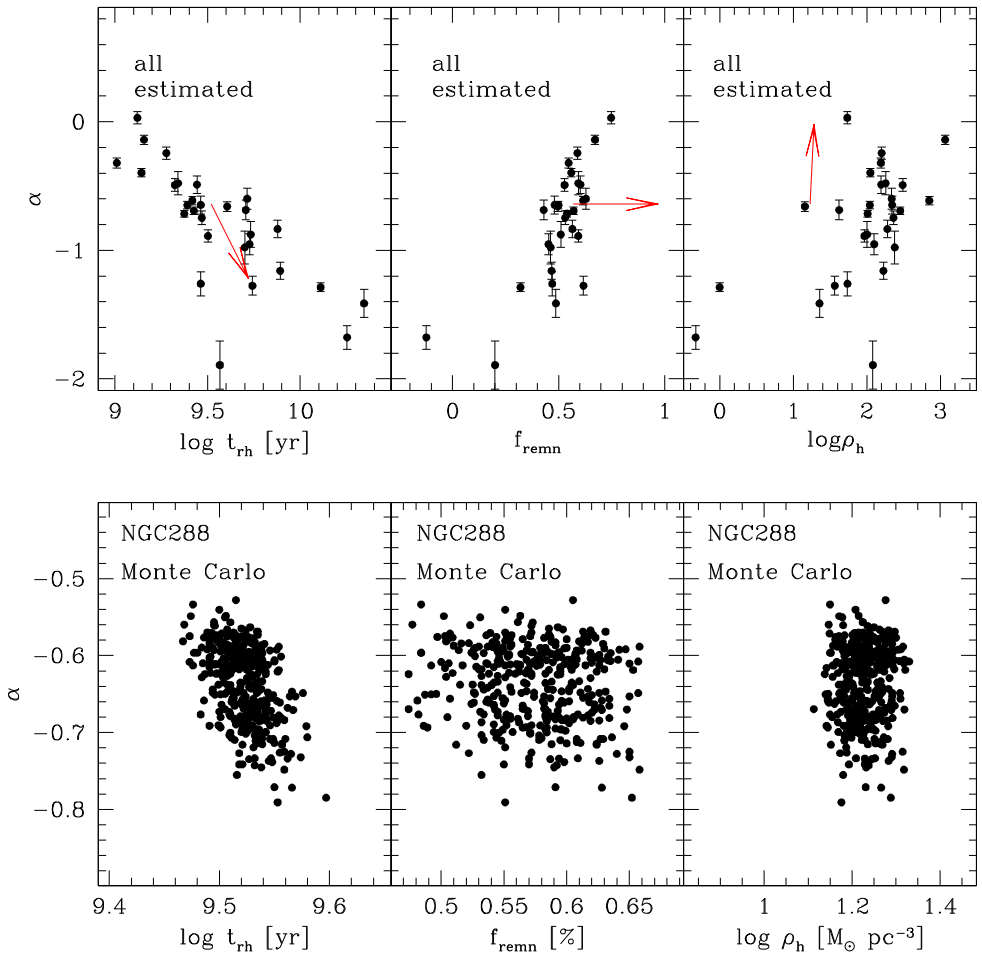

Figure 12. Bottom panels: distribution of the accepted trials of the Markov Chain Monte Carlo in the logt_{rh}–α (left), f_{remn}–α (middle) and logρ_h–α (right) planes. Top panels: distribution of the 29 analysed clusters in the logt_{rh}–α (left), f_{remn}–α (middle) and logρ_h–α (right) planes. The orientation of the biases are indicated by arrows.

logt_{rh} as the independent variable. To estimate how significant the improvement with respect to an univariate fit is, we applied the same Monte Carlo approach described above: we compared the χ^2 of the bivariate fit (assuming logt_{rh} as the first independent variable) with those obtained by randomly swapping the values of the adopted second independent variable. We found a marginally significant (P = 97.7 per cent) improvement with respect to the univariate fit only by assuming as second independent variable f_{remn}.

Unfortunately, t_{rh}, f_{remn}, ρ_h and α are all output parameters of the best-fitting multimass model adopted in this work. It is therefore possible that covariances between the uncertainties in these parameters conspire to spuriously create the quoted correlations. To test this hypothesis, we run a Markov Chain Monte Carlo analysis on our target GCs. This algorithm samples the parameter space in the neighbourhood of the best-fitting parameters, providing a distribution of accepted trials which reflect the actual probability distribution. The distribution of accepted trial values in the logt_{rh} − α, f_{remn} − α and logρ_h–α planes for the cluster NGC 288 are shown in Fig. 12, as an example. The covariance between α and logt_{rh} is apparent with a tendency of solutions with longer t_{rh} to have shallower MFs, while no significant slope with logρ_h or f_{remn} is noticeable. A similar behaviour has been noticed in the other clusters with no significant dependence of the bias orientation and strength on the position in these planes. Note that the direction of such a bias in the logt_{rh}–α plane is similar to that of the observed correlation. However, the shift in α along the bias direction needed to erase any significant correlation with logt_{rh} would be as large as $\Delta\alpha \sim 0.8$ at the extreme of this plot i.e. ∼3 times larger than typical uncertainties. To further check that the observed correlation is not driven by the covariance spuriously introduced by the adopted fitting procedure, we correlated the derived MF slopes with the logt_{rh} values derived independently by McLaughlin & van der Marel (2005) fitting single-mass King (1966) models. Also in this case, we found a confidence level >99.9 per cent that the two variables are correlated. So, while it is conceivable that the observed logt_{rh}–α correlation is sharpened by the covariance between errors, it cannot be completely produced by this bias.

Another source of bias could be linked to an overestimate of the level of completeness. This could indeed spuriously deplete the MF at its low-mass end, in particular for dense GCs characterized by short relaxation times. While we cannot completely exclude this occurrence, it is unlikely that a significant bias in the estimated completeness is present above the magnitude limit corresponding to stellar masses $m > 0.2\,M_\odot$, in the portion of the CMD used to estimate the MF slope. To check the possible effect of uncertainties in the completeness correction, we repeated the analysis by using the MF slope α calculated assuming a high $m > 0.3\,M_\odot$ cut and excluding all those clusters with completeness levels <50 per cent within their core radii at masses <0.25 $M_\odot$ (see Leigh et al. 2012). Although only 15 GCs survive to this severe criterion, the

correlation between α and $\log t_{\rm rh}$ remains significant at 99.9 per cent, while the significance levels of the other correlations drop below 75 per cent. On the basis of the above test, we conclude that the $\log t_{\rm rh}$–α correlation we observe among the GCs of our sample is robust and real.

7 DISCUSSION

Through a comparison of the deepest available *HST* photometric data with multimass King–Michie models, we derived the MFs of 35 Galactic GCs just above the hydrogen-burning limit as well as structural parameters, masses, *M/L* ratios and fraction of remnants for a subset of 29 GCs with available radial velocity information.

The MFs of GCs are generally well described by power laws, in particular when clusters with relatively shallow MF slopes ($\alpha > -1$) are analysed. Noticeable deviations from power laws are evident in clusters whose MFs are steeper than $\alpha = -1$. In particular, in these cases a bend in the MF is appreciable at masses $m \sim 0.4\,{\rm M}_{\odot}$ with a significant depletion of low-mass stars. This evidence has been previously reported by De Marchi & Paresce (1997) and De Marchi, Paresce & Portegies-Zwart (2010), who also defined a relation linking the position of the bend with the dissolution time-scale. These GCs have half-mass relaxation times of $t_{\rm rh} > 6$ Gyr, and it is possible that their MFs have not been significantly altered by dynamical evolution effects. We will discuss these deviations in greater detail in a second paper (Baumgardt & Sollima 2017), where we compare the MF slopes derived in this work with the results of *N*-body simulations. In this interpretation, the convex shape of their MFs might resemble the original shape of the IMF, in agreement with the prediction of Kroupa (2001) and Chabrier (2003).

By correlating the derived MF slopes with different structural and orbital cluster parameters, we found significant and tight correlations with the half-mass relaxation time. Although covariance between uncertainties can spuriously enhance the strength of the $\log t_{rh}$–α correlation, we believe that it is real since (i) its extent exceeds the range over which the above-mentioned bias would produce a sizeable effect, and (ii) it is significant using independent estimates of $t_{\rm rh}$. This correlation is expected as a result of the natural evolution of collisional stellar systems. Indeed, two-body relaxation is the main mechanism leading to the segregation of low-mass stars to the outer cluster parts, where they can be easily lost by tidal stripping (Vesperini & Heggie 1997; Baumgardt & Makino 2003; Leigh et al. 2012). So, the shorter the time-scale of internal dynamical evolution the more efficient is the depletion of the MF. However, the location of *N*-body simulations in the $\log t_{\rm rh}$–α plane is highly sensitive to the original slope of the IMF, with clusters starting with a steeper IMF reaching also steeper present-day MFs after a given number of elapsed relaxation times than clusters starting with flatter IMFs (Webb & Vesperini 2016). Thus, a significant spread in this relation would be apparent if cluster-to-cluster variations of the IMF were present at the epoch of their formation. On the other hand, all surveys of *N*-body simulations performed so far, showed that two-body relaxation is expected to produce a slow variation of the MF slope. In particular, simulations starting with a Kroupa (2001) IMF take ∼13 half-mass relaxation times to flatten their MF up to a slope of $\alpha = -1$ and reach a flat $\alpha = 0$ slope only close to dissolution (Baumgardt & Makino 2003; Webb & Vesperini 2016; Lamers et al. 2013). In such a picture, it is hard to explain the large range in α covered by the GCs of our sample, in particular in the less-evolved $t_{\rm age}/t_{\rm rh} < 5$ regime, without any primordial spread in their IMFs. In this last case, however, a correlation between the IMF slope and the present-day half-mass relaxation time would be necessary to reproduce the observed $\log t_{\rm rh}$–α correlation.

The universality of the IMF of Milky Way GCs has important implications for the thermodynamics of the gas clouds from which GCs formed at high redshift. Theoretical arguments indeed suggest a dependence of the IMF on the metal content and the initial density of the cluster because of their effect on the Jeans mass and on the efficiency of radiative feedback (Silk 1977; Adams & Fatuzzo 1996; Larson 1998; Klessen, Spaans & Jappsen 2007), although the actual impact of these processes is uncertain. Whether Milky Way GCs were born with a universal IMF or not, provides insight on the efficiency of these mechanisms in the environmental conditions of GCs at their birth. It is interesting to consider the evidence found in stellar systems populating regions of the $M_{\rm V}$–$r_{\rm eff}$ plane contiguous to GCs. In this regard, while Grillmair et al. (1998) and Wyse et al. (2002) derived MFs for Draco and Ursa Minor dwarf spheroidals which are consistent with a Salpeter (1955) IMF, Geha et al. (2013) found evidence of MF variations correlated with the mean metallicity in a sample of ultrafaint dwarf galaxies. Since these systems are dynamically unevolved, these variations can be only interpreted as primordial. This study has been however questioned by El-Badry, Weisz & Quataert (2017), who found that significant MF differences cannot be detected unless the photometric data used are significantly deeper than that currently available. On the other hand, Weisz et al. (2013) analysed a large sample of young clusters and associations whose MFs are available in the literature. In spite of the large cluster-to-cluster differences, a careful revision of the associated errors indicates that the hypothesis that they are consistent with a single IMF slope cannot be ruled out. Hence, due to the above conflicting results, it is not clear if a common mechanism of star formation was at work for GCs and less massive and dense stellar systems.

Interestingly, Baumgardt & Makino (2003), Lamers et al (2013) and Webb & Leigh (2015) found a unique relation linking the present-day MF slope and the fraction of mass lost by their simulated GCs. Such a relation, which is valid only if a universal IMF is assumed, appears to be almost insensitive to the strength of the tidal field, the type of cluster orbit, and to the initial mass and size of the cluster. The MFs derived here have slopes which imply a huge amount of mass lost (>70 per cent) by the majority of GCs in our sample. By inverting equation (14) of Baumgardt & Makino (2003) and adopting the present-day masses listed in Table 1, we estimated the amount of mass lost by each cluster during its evolution. Assuming that our sample covers ∼20 per cent of the GC system of the Milky Way, a global mass of $\sim 2 \times 10^8\,{\rm M}_{\odot}$, mainly in low-mass stars, could have been released in the Galactic halo by GCs. In spite of the large uncertainties in the Galactic halo mass (Morrison 1993; Bell et al. 2008; Deason, Belokurov & Evans 2011), this could constitute a significant contribution to the total mass budget of the halo. This is in agreement with the prediction by Martell & Grebel (2010) based on the fraction of halo stars showing the chemical signature of GCs stars. In this picture, one would expect a significant excess of low-mass stars in the MF of halo stars. Such a prediction could be probably verified by the incoming data provided by the *Gaia* survey.

Another significant correlation has been found between the present-day MF slopes and the fraction of dark mass. The natural interpretation of this correlation is that dark remnants (mainly constituted by white dwarfs) have masses larger than the average cluster stars and are being more efficiently retained. Moreover, the fraction of white dwarfs steadily increase with time as less massive (and more abundant) stars approach this late stage of their evolution.

Studies based on *N*-body simulations have shown that, because of the two above-mentioned processes, the fraction of mass contained in remnants increases as two-body relaxation proceeds (Baumgardt & Makino 2003; Contenta, Varri & Heggie 2015). Such a correlation becomes less significant when dense GCs, subject to low completeness at low masses are excluded.

Significant correlations with the half-mass and (marginally) with the central density (obviously related to $t_{\rm rh}$) have also been found, in agreement with previous finding by Paust et al. (2010). All the correlations with orbital parameters and position in the Galaxy suggested by previous studies based on the analysis of small samples of GCs (Capaccioli et al. 1993; Djorgovski et al. 1993; Piotto & Zoccali 1999), have been found to be less significant although they cannot be completely ruled out. No significant correlation has been found with the cluster concentration, as previously suggested by De Marchi et al. (2007). Note that, while the uncertainties on the individual MF slopes do not allow us to exclude the presence of such a correlation, for most GCs studied by De Marchi et al. (2007), the slope of the global MF has been assumed to be that measured in an external region close to the half-mass radius. However, in high-concentration clusters, the analysed fields are often located well beyond the half-mass radii estimated here, a region where the MF is expected to be steeper because of mass-segregation effects. In particular, there are three high-concentration GCs out of 6 in their sample where the MF is calculated between 3 and 7 half-mass radii. This could create a spurious correlation between MF slope and concentration.

It is worth stressing that our results are based on an analysis conducted in the central region of GCs where mass-segregation effects are particularly strong. As a consequence, the derived global MFs are sensitive to the recipe of mass segregation of the adopted multimass models. In Sollima et al. (2015), we showed that such an assumption can potentially lead to biases in the estimated MF slopes as large as $\Delta\alpha \sim 0.2$, i.e. comparable with the estimated random uncertainties (see Section 5). Although the magnitude of such a bias cannot alter the conclusions of this paper, the present analysis would greatly benefit from constraints on the MF measured in the outer regions of these clusters (see e.g. Sollima et al. 2017).

ACKNOWLEDGEMENTS

We warmly thank Michele Bellazzini, Enrico Vesperini and Luca Ciotti for useful discussions. We also thank the anonymous referee for his/her helpful comments and suggestions.

REFERENCES

Adams F. C., Fatuzzo M., 1996, ApJ, 464, 256
Allen C., Moreno E., Pichardo B., 2006, ApJ, 652, 1150
Allen C., Moreno E., Pichardo B., 2008, ApJ, 674, 237
Alonso-García J., Mateo M., Sen B., Banerjee M., Catelan M., Minniti D., von Braun K., 2012, AJ, 143, 70
Anderson J. et al., 2008, AJ, 135, 2055
Bastian N., Covey K. R., Meyer M. R., 2010, ARA&A, 48, 339
Baumgardt H., 2017, MNRAS, 464, 2174
Baumgardt H., Sollima A., 2017, MNRAS, in press
Baumgardt H., Makino J., 2003, MNRAS, 340, 227
Bell E. F. et al., 2008, ApJ, 680, 295
Bonnell I. A., Bate M. R., Clarke C. J., Pringle J. E., 1997, MNRAS, 285, 201
Calamida A. et al., 2015, ApJ, 810, 8
Capaccioli M., Piotto G., Stiavelli M., 1993, MNRAS, 261, 819
Chabrier G., 2003, PASP, 115, 763
Chabrier G., Mera D., 1997, A&A, 328, 83
Contenta F., Varri A. L., Heggie D. C., 2015, MNRAS, 449, L100
Da Costa G. S., 1982, AJ, 87, 990
De Marchi G., Paresce F., 1997, ApJ, 476, L19
De Marchi G., Paresce F., Pulone L., 2007, ApJ, 656, L65
De Marchi G., Paresce F., Portegies Zwart S., 2010, ApJ, 718, 105
Deason A. J., Belokurov V., Evans N. W., 2011, MNRAS, 416, 2903
Djorgovski S., King I. R., 1984, ApJ, 277, L49
Djorgovski S., Piotto G., Capaccioli M., 1993, AJ, 105, 2148
Dotter A., Chaboyer B., Jevremović D., Baron E., Ferguson J. W., Sarajedini A., Anderson J., 2007, AJ, 134, 376
Dotter A. et al., 2010, ApJ, 708, 698
El-Badry K., Weisz D. R., Quataert E., 2017, MNRAS, 468, 319
Fleck R. C., Jr, 1982, MNRAS, 201, 551
Geha M. et al., 2013, ApJ, 771, 29
Giersz M., Heggie D. C., 1996, MNRAS, 279, 1037
Grillmair C. J. et al., 1998, AJ, 115, 144
Gunn J. E., Griffin R. F., 1979, AJ, 84, 752
Harris W. E., 1996, AJ, 112, 1487
Kalirai J. S., Saul Davis D., Richer H. B., Bergeron P., Catelan M., Hansen B. M. S., Rich R. M., 2009, ApJ, 705, 408
King I. R., 1966, AJ, 71, 64
Klessen R. S., Spaans M., Jappsen A.-K., 2007, MNRAS, 374, L29
Kroupa P., 2001, MNRAS, 322, 231
Kruijssen J. M. D., 2009, A&A, 507, 1409
Lamers H. J. G. L. M., Baumgardt H., Gieles M., 2013, MNRAS, 433, 1378
Larson R. B., 1998, MNRAS, 301, 569
Leigh N., Umbreit S., Sills A., Knigge C., de Marchi G., Glebbeek E., Sarajedini A., 2012, MNRAS, 422, 1592
Martell S. L., Grebel E. K., 2010, A&A, 519, A14
McClure R. D. et al., 1986, ApJ, 307, L49
McLaughlin D. E., van der Marel R. P., 2005, ApJS, 161, 304
Melbourne J., Sarajedini A., Layden A., Martins D. H., 2000, AJ, 120, 3127
Miller G. E., Scalo J. M., 1979, ApJS, 41, 513
Miocchi P. et al., 2013, ApJ, 774, 151
Morrison H. L., 1993, AJ, 106, 578
Nakamura F., Umemura M., 2001, ApJ, 548, 19
Paresce F., De Marchi G., 2000, ApJ, 534, 870
Paust N. E. Q. et al., 2010, AJ, 139, 476
Paust N., Wilson D., van Belle G., 2014, AJ, 148, 19
Piotto G., Zoccali M., 1999, A&A, 345, 485
Pulone L., De Marchi G., Covino S., Paresce F., 2003, A&A, 399, 121
Richer H. B., Fahlman G. G., Buonanno R., Fusi Pecci F., 1990, ApJ, 359, L11
Robin A. C., Reylé C., Derrière S., Picaud S., 2003, A&A, 409, 523
Salpeter E. E., 1955, ApJ, 121, 161
Santiago B. X., Elson R. A. W., Gilmore G. F., 1996, MNRAS, 281, 1363
Sarajedini A. et al., 2007, AJ, 133, 1658
Silk J., 1977, ApJ, 214, 718
Sollima A., Bellazzini M., Lee J.-W., 2012, ApJ, 755, 156
Sollima A., Baumgardt H., Zocchi A., Balbinot E., Gieles M., Hénault-Brunet V., Varri A. L., 2015, MNRAS, 451, 2185
Sollima A., Dalessandro E., Beccari G., Pallanca C., 2017, MNRAS, 464, 3871
Trager S. C., King I. R., Djorgovski S., 1995, AJ, 109, 218
Vesperini E., Heggie D. C., 1997, MNRAS, 289, 898
Watkins L. L., van der Marel R. P., Bellini A., Anderson J., 2015, ApJ, 803, 29
Webb J. J., Leigh N. W. C., 2015, MNRAS, 453, 3278
Webb J. J., Vesperini E., 2016, MNRAS, 463, 2383
Weisz D. R. et al., 2013, ApJ, 762, 123
Wyse R. F. G., Gilmore G., Houdashelt M. L., Feltzing S., Hebb L., Gallagher J. S., III, Smecker-Hane T. A., 2002, New Astron., 7, 395
Zoccali M., Cassisi S., Frogel J. A., Gould A., Ortolani S., Renzini A., Rich R. M., Stephens A. W., 2000, ApJ, 530, 418
Spitzer L., 1987, Dynamical Evolution of Globular Clusters. Princeton Univ. Press, Princeton

This paper has been typeset from a TEX/LATEX file prepared by the author.